Article

Eccentric Rotor Drop Dynamics Study of Vertical Maglev Bearing System

Xiaoxu Pang [1,2,*], Dingkang Zhu [1,*], Ming Qiu [1,2,3], Dongfeng Wang [4] and Xinlong Wang [1]

[1] School of Mechanical and Electrical Engineering, Henan University of Science and Technology, Luoyang 471003, China
[2] High-Level Bearing Henan Synergy Innovation Center, Luoyang 471003, China
[3] Henan Collaborative Innovation Center for Advanced Manufacturing of Machinery and Equipment, Luoyang 471003, China
[4] Luoyang Bearing Science & Technology Co., Ltd., Luoyang 471003, China
[*] Correspondence: pxx8308@163.com (X.P.); zdkkong@163.com (D.Z.)

Abstract: When considering the problem of a vertical magnetic levitation bearing system, the rotor eccentric fall is more likely to cause the failure of the protective bearing. In this paper, a rotor drop collision model and a protective bearing dynamics model are constructed. It compares and analyzes the evolution of collision force values of the rotor eccentric drop as well as the non-eccentric drop. Further, this paper discusses the law of influence of three factors, rotor quality, rotational speed, and axial protection clearance, on the collision characteristics of the protected bearing in eccentric and non-eccentric cases. It has also experimentally verified this characteristic of rotor speed. The results show that compared with the non-eccentric condition, the axial impact force and radial impact forces of the rotor in the eccentric condition increase by 14% and 114%, respectively. Compared with the non-eccentric condition, with the increase in rotor quality, the axial and radial impact force increase by 68% on average, and the axial depth amplitude of the rotor increases by 350%. With the increase of rotor speed, the axial impact force without an eccentric drop is basically unchanged; the axial impact force of an eccentric drop increases slightly, and the radial impact force increases by 110%. With the increase of axial protection clearance, the radial displacement vibration of the rotor axis increases; the average increase of the maximum axial force is 120 N, and the average increase of the maximum radial force is 100%.

Keywords: vertical magnetic levitation system; protective bearing; collision characteristics; eccentric drop

1. Introduction

The magnetic suspension bearing can suspend the rotor with the magnetic field force without lubrication and friction and can use the unbalanced compensation method to control and optimize the rotor position using a high-precision system [1]. It is a mechatronics support device [2] that can be applied and can realize active control.

After the failure of the magnetic levitation system, the rotor and the bearing inner ring will cause a huge vibration impact, and the bearing roller will slip and lead to rubbing wear. In 1997, when the EC conducted the experiment on the aero-engine with the magnetic suspension bearing system at 18,000 r/min, the 150 kg rotor fell to the protective bearing due to the failure of the magnetic suspension system, resulting in a huge impact. This led to the breakage of the protective bearing and severe damage to the magnetic levitation bearing system [3].

2. Literature Review

As an important line of defense to protect the whole machine after the magnetic suspension system fails, the protective bearing can make a passive response when the system

fails. In order to improve the drop resistance of the protective bearing and the reliability during service, it is necessary to study the dynamics of the collision of the rotor falling into the protective bearing. Heshmatallah Mohammad Khanlo et al. [4] studied the contact force between the inner axis and the auxiliary bearing and revealed various nonlinear dynamical behaviors, such as periodic, quasi-periodic, periodic, and chaotic vibrations, and jumping phenomena. The results show that the speed parameters, axial speed ratio, and gravity parameters have a significant impact on the dynamic response. Wu Guoqing et al. [5] studied the support structure of the maglev wind turbine and constructed a drop simulation model to explore the influence of different structural parameters of protective bearing on the rotor track. Kong Yanan et al. [6] simulated the rotor drop process of the magnetic bearing system to explore the influence trend of the eccentric rotor speed and dynamic balance accuracy level on the drop collision force. Zhu Yili et al. [7] proposed using the elastic ring to buffer the shock and vibration caused by the rotor drop and to simulate the drop model under different installation positions of the rotor. The results show that increasing the elastic ring on the rotor can effectively reduce the collision force and amplitude during the drop. Wei Peng et al. [8] simulated the drop collision force of the rotor at high speed, explored the test machine, and gave a method to measure the collision force. Zhao Jingxiong et al. [9] used finite element software to simulate the rotor drop process, explored the collision characteristics of the auxiliary bearing in the helium fan experimental bench, and analyzed the intrusion depth and wear influence between the bearing inner ring and the rolling body. Patrick S. Keogh et al. [10] studied the transient thermal response of protective bearings, and the results showed that this method had some reference value for predicting the life span of protective bearings. Ma Zilin [11] selected full-loaded ceramic ball angular contact bearings without cages as protective bearings for horizontal magnetic bearing systems. This paper analyzed the rotation speed of the inner ring of the bearing, the axial collision force of the inner ring, the contact force between adjacent spheres, and the sliding speed of the raceway between the ball and the inner ring during the rotor dropping process and concluded that the fully-loaded ceramic ball has the margin to bear further load at high speed. Lin Ma et al. [12] established a dynamic model of the rotor and the protective bearing. They analyzed the dynamic behavior of the axis trajectory diagram through the three-dimensional bifurcation diagram and two-parameter bifurcation diagram, optimized the structural parameter design of the rotor system, and determined its reasonable and stable working interval. Yang Guojun et al. [13] discussed the design characteristics of the magnetic bearing control system of HTR-10GT and then studied the influence of AMB stiffness on the critical speed of the rotor. Zhu Changsheng [14] established the active electromagnetic bearing internal rotor in the finite element method as the basis of kinematics formulas, mainly analyzing the maglev bearing after the failure of the rotor drop dynamics, generally for the instantaneous nonlinear characteristics, and discussed the application of protective bearing support damping and support stiffness. Li [15] designed the vertical magnetic bearing system by using two kinds of protective bearings with a full ball and a cage without a cage to conduct a rotor drop simulation, analyzed the internal temperature rise of bearings, rotor drop space trajectory, and the influence of changes in axial and radial contact forces, and finally concluded that the ceramic ball hybrid bearing with a cage was a more suitable anti-impact scheme.

Many achievements have been made in the research of rotor falling under non-eccentric conditions after the failure of the maglev bearing system, but research on rotor falling dynamics with an eccentric angle is scarce. However, due to the inherent disorder of the magnetic levitation bearing system during high-speed operation and the problem of low control accuracy, the rotor is in a state of inclined rotation and revolution motion superposition. Therefore, in the actual manufacturing or motor-driven rotor high-speed rotation, the rotor drop under the eccentric condition is more practical. In this paper, we investigate the eccentric rotor drop dynamics of the vertical magnetic levitation system that is more in line with the actual working conditions; it constructs a rotor drop collision model and a protective bearing dynamics model. This paper makes a comparison of the magnitude of

the collision force between the rotor drop and the protective bearing under eccentric and non-eccentric conditions, and the effect of different operating parameters of the rotor on the collision force and the radial displacement of the rotor axis is also investigated.

3. Research Methodology

3.1. Working Principle of Vertical Maglev Bearing System

Figure 1 is the vertical maglev bearing system structure diagram. The model is composed of a rotor, motor, two radial magnetic bearings, a group of symmetrical configurations of axial magnetic bearings, upper and lower protective bearings, and an upper collision adjustment pad. In this paper, considering the rotor eccentricity, high-speed heavy load, and large impact load conditions, the 71913C angular contact ball bearing (without cage) is installed face to face as the upper protective bearing, bearing the main axial and radial impact forces. The lower protective bearing is a 61809 deep groove ball bearing, which only bears part of the radial impact force to reduce the rotor swing amplitude when the rotor swings inertia, and only plays a radial protection role. The specific parameters of the two bearings are shown in Table 1:
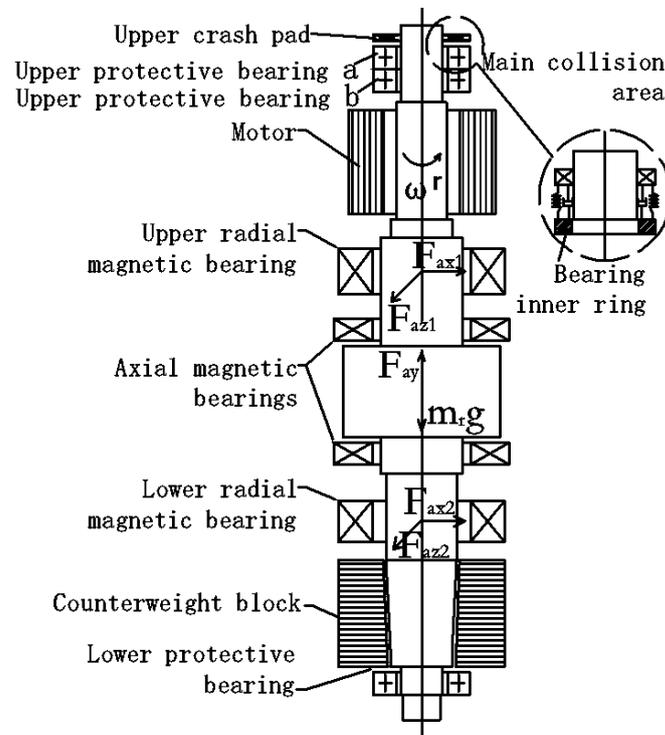
Figure 1. Schematic diagram of a shaft system structure of vertical magnetic levitation bearing system.

Table 1. Input boundary conditions.

Type	Model Number	Bore Diameter (mm)	Outside Diameter (mm)	Width (mm)	Cr (kN)	Cor (kN)
Deep groove ball bearing	61809	45	58	7	6.40	5.60
Angular contact ball bearing	71913C	65	90	13	20.8	21.2

The outer ring of the protective bearing of the upper and lower parts of the rotor of the maglev bearing system is placed on a special tooling, and the inner ring is in a stable state under gravity (in the simplified model, it is considered that the outer ring is in a fixed state and the inner ring is in a floating state). In normal operation, the rotor is suspended

by the magnetic force of axial and radial magnetic bearings, and the motor drives the rotor to rotate at high speed. The weight of the whole rotor can be changed by increasing or decreasing the weight of the counterweight block so as to analyze different working conditions. However, due to the performance and accuracy problems of the magnetic bearing control system, the magnetic bearing disconnection caused by the control failure will cause the rotor to drop off in high-speed rotation, so the protective bearing is set as an efficient defense line to avoid the rotor collision and damage the whole machine. There is a gap between the upper and lower protective bearings and the rotor without force action. At this time, the force of the rotor is gravity $m_r g$, the upper and lower radial magnetic bearing support forces F_{ax} and F_{az}, and the axial magnetic bearing supports force F_{ay}. The falling rotor colliding with the inner ring of the protective bearing will produce complex nonlinear behavior on the axial displacement and collision force of the rotor, so the analysis of nonlinear multi-factor coupling dynamics becomes complex [16–18]. The following mathematical model is established for this.

3.2. The Collision Model between the Rotor and the Protective Bearing

In the collision process, the rotor is assumed to be a rigid body. Only elastic deformation occurs after the collision between the rotor and the inner ring of the protective bearing, and the collision process can be converted into a spring-damping model.

The mechanical calculation formula of the linear spring is

$$F_n = kx + c\dot{x} \tag{1}$$

where k is the contact stiffness, c is the contact damping, and x is the deformation degree. The linear mathematical model presented in this paper is sufficient to evaluate the amplitude-frequency response of a magnetic bearing under multi-frequency excitation of a rotor drop collision by self-programming a multi-degree-of-freedom magnetic levitation nonlinear energy acquisition system formed by adding linear spring vibrators [19,20].

Figure 2a is the schematic diagram of the position of the rotor and the rolling bearing, where o is the coordinate origin, namely, the equilibrium position of the stable suspension of the rotor. Furthermore, o_1 is the rotor axis; set the initial unilateral gap between the rotor and the bearing inner ring to be s, and the intrusion depth of the rotor and the inner ring to be τ_1:

$$\tau_1 = \sqrt{(x_r - x_{b1})^2 + (z_r - z_{b1})^2} - s \tag{2}$$

(a)   (b)
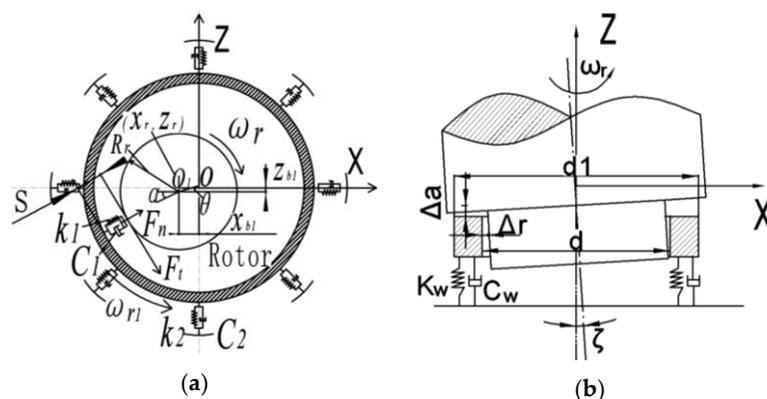
Figure 2. Simplified collision model of rotor and protective bearing. (**a**) Radial collision; (**b**) axial impact.

The relative compression deformation between the bearing inner ring and the steel ball is τ_2:

$$\tau_2 = \sqrt{{x_{b1}}^2 + {z_{b1}}^2} \tag{3}$$

where the axis-coordinate value of the rotor is (x_r, z_r). x_{b1} is the offset of the bearing hub axis X direction. z_{b1} is the offset of the bearing inner ring axis in the Z direction.

When $\tau_1 > 0$, the rotor is in contact with the inner ring of the bearing, and then the rotor will receive radial contact force and tangential friction force from the inner ring on the contact surface. A relevant equation of state can be obtained using force analysis on the rotor:

$$m_r \ddot{x}_r = -F_{n1} \cos \alpha' - F_{t1} \sin \alpha' \tag{4}$$

$$m_r \ddot{z}_r = -m_r g + F_{t1} \cos \alpha' - F_{n1} \sin \alpha' \tag{5}$$

$$\alpha' = -\arctan \frac{z_r - z_{b1}}{x_r - x_{b1}} \tag{6}$$

where F_{n1} is the radial contact force between the rotor and the bearing inner ring, F_{t1} is the tangential friction between the rotor and the bearing inner ring, and α' is the contact phase angle between the rotor and the bearing inner ring.

We analyzed the torque balance of the rotor. In the contact stage, relative to the axis, the balanced rotor is subjected to friction torque, so there is

$$J_r \ddot{\theta}_r = -F_{t1} R_r \tag{7}$$

According to the spring damping system model, the contact force between the rotor and the inner ring can be expressed as

$$F_{n1} = k_1 \tau_1^{e_1} + c_1 V_{n1} \tag{8}$$

$$V_{n1} = \frac{(\dot{x}_r - \dot{x}_{b1})(x_r - x_{b1}) + (\dot{z}_r - \dot{z}_{b1})(z_r - z_{b1})}{\sqrt{(x_r - x_{b1})^2 + (z_r - z_{b1})^2}} \tag{9}$$

where k_1 is the radial contact stiffness coefficient between the rotor and the bearing inner ring; e_1 is the contact coefficient; c_1 is the contact damping between the rotor and the bearing inner ring; and V_{n1} is the normal velocity of the rotor opposite to the bearing inner ring. The contact stiffness coefficient can be solved according to the calculation method of line contact in Hertz's theory [21]. According to the simplified model, the collision contact between the rotor and the inner ring can be considered the contact between the rotor and the fixed ring. When the material between the rotor and the fixed ring is steel, the contact width between them is the width of the inner ring end face l = 3.5 mm: $k_1 = 3.378 \times 10^8$ (N/mm), $e_1 = 10/9$.

In addition, research on damping has not yet formed a relatively mature calculation method, and damping parameters are generally obtained by testing. Here, contact damping is commonly used [10]: $c_1 = 1000$ (N·s/mm)

Figure 2b is the axial collision model. K_w is supporting stiffness; C_w is the contact damping; Δa is the axial protection gap; Δr is the radial protection gap; ζ is the rotor eccentric angle; k_t is the eccentric angle fixed constant; d is the bearing bore diameter; and d_1 is the diameter of the inner ring retaining edge.

The axial collision force is

$$F_a = K_{ca}(|l_a - l_{ia}| - \Delta_a) \cos(k_t - \zeta) \tag{10}$$

$$K_{ca} = 1.2 \times 10^{11} \sqrt{\pi(d_1^2 - d^2)} \tag{11}$$

In formula: l_a is the axial displacement of the rotor, and l_{ia} is protecting the axial displacement of the bearing inner ring.

3.3. Dynamics Model of Protective Bearings

The relative displacements of the inner and outer rings in radial and axial directions are τ_r and τ_a, respectively. We specify that the position of the scroll is $\theta = 0$. Figure 3 shows the center of the ball and the curvature of the inner and outer grooves. After any steel ball is loaded, the axis and radial coordinates of the curvature center of the inner groove Q'_{da} at position θ_a are [22]:

$$A_{ya} = BD_W \sin \alpha + \tau_a \tag{12}$$

$$B_{ya} = BD_W \cos \alpha + \tau_r \cos \theta_q \tag{13}$$

where: D_W is the bearing steel ball diameter; $B = g_q - 1 + g_w$, g_q, g_w, respectively, is the inner and outer ring of the groove radius of curvature coefficient; general ball bearing g value between 0.52~0.53; α is the contact angle before loading.
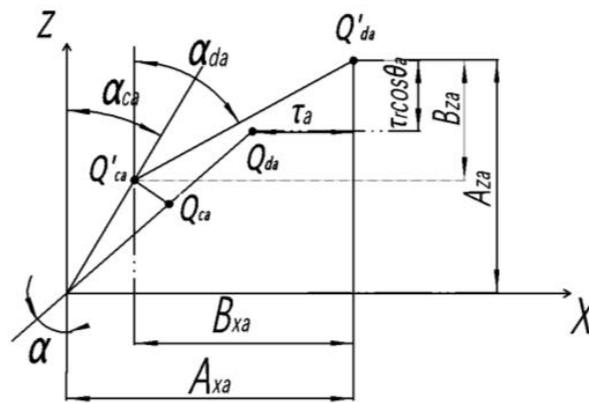

Figure 3. The position of the center of a steel ball relative to the center of curvature of the groove.

The deformation of the steel balls is, respectively,

$$\tau_{ca} = Q'_{ca}Q'_{da} - Q_{ca}Q_{da} = \sqrt{B_{xa}^2 + B_{za}^2} - (g_q - 0.5)D_W \tag{14}$$

$$\begin{aligned} \tau_{da} &= Q'_{ca}Q'_{da} - Q_{ca}Q_{da} \\ &= \sqrt{(A_{xa} - B_{xa})^2 - (A_{za} - B_{za})^2} - (g_w - 0.5)D_W \end{aligned} \tag{15}$$

In this formula, B_{xa} is the force, and B_{za} is the speed; Q_{ca} and Q_{da} are the center of the ath steel ball before the load and the corresponding curvature center. Because the outer ring is fixed, the center of curvature Q'_{ca} does not change, and Q'_{ca} and Q'_{da} are the center of the ath steel ball and the corresponding center of curvature after being loaded, respectively.

The contact load of the steel ball and the inner and outer loops is

$$Q_{da} = K_{da}\tau_{da}^{\frac{3}{2}} \tag{16}$$

$$Q_{ca} = K_{ca}\tau_{ca}^{\frac{3}{2}} \tag{17}$$

where: K_{da} and K_{ca} can be calculated from formula (5-5) in literature [23], and their values are related to the contact angle.

The contact angle of the ath steel ball and the inner and outer ring rolling path is

$$\cos \alpha_{da} = \frac{B_{za}}{(g_q - 0.5)D_W + \tau_{da}} \tag{18}$$

$$\cos \alpha_{da} = \frac{B_{xa}}{(g_q - 0.5) D_W + \tau_{da}} \tag{19}$$

$$\cos \alpha_{ca} = \frac{A_{za} - B_{za}}{(g_w - 0.5) D_W + \tau_{ca}} \tag{20}$$

$$\sin \alpha_{da} = \frac{A_{xa} - B_{za}}{(g_q - 0.5) D_W + \tau_{da}} \tag{21}$$

4. Results

4.1. Comparative Analysis of Collision Characteristics under Non-Eccentric and Eccentric Working Conditions

The simplified rotor drop collision model of the vertical magnetic suspension bearing system is simulated and analyzed by using self-programming multi-body dynamics software. That is, the multivariate nonlinear second-order differential equations obtained from the above simultaneous equations were solved by using the Runge-Kutta method of 4–5 orders. The calculation accuracy was set as 1×10^6, and the solution was solved from the rotor to 0.5 s after the drop. Due to the large axial impact force caused by the vertical fall of the vertical rotor, the bearing outer ring is set with a fixed pair to be pre-tightened and fixed to prevent the axial displacement of the protective bearing outer ring. Moreover, the upper collision pad is fixed on the rotor in the form of a fixed pair. The simulated radial protection gap is 0.2 mm, and the contact stiffness is 1×10^5; the contact damping is 70; the coefficient of dynamic friction and static friction are 0.1 and 0.3, respectively, and the time is 0.4 s or 0.5 s. In the subsequent analysis, the above initial input parameters are used for dynamic simulation analysis.

Figure 4 shows a simplified schematic diagram of the rotor movement under eccentric working conditions. The rotor coupled the rotational and rotational motion states, which were superimposed on each other and acted on the axis locus together [24–26]. Most of the axial impact force in the upper angle contact ball bearing group is borne by protective bearing *a*. Rotor axis displacement, protective bearing an inner ring, shaft between rotors, and radial impact force are the main research parts of this paper.
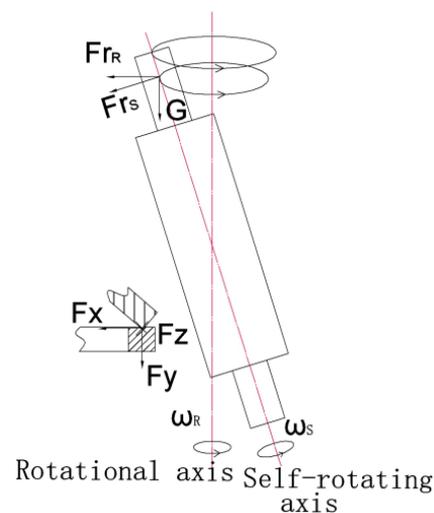

Figure 4. Schematic diagram of the rotor simplified model under eccentric working conditions.

Due to the large distance between the radial plane of the rotor axis and the radial plane of the protective bearing *a*, there is a motion phase difference between the displacement at the rotor axis and that at the protective bearing *a*. Therefore, this paper does not study the displacement at the rotor axis, and the axis studied in this paper is the axis that protects a bearing a with the radial plane. The rotor drop axis displacement and

impact force under eccentric conditions are more in line with the actual conditions. The following is a comparative analysis of the impact characteristics of the rotor that falls under non-eccentric conditions.

Figures 5–7 are comparative analyses of non-eccentric and eccentric conditions under the rotating speed of 20,000 r/min, axial and radial protection clearance of 0.2 mm, 45 kg rotor, and eccentric angle of 0.05°.
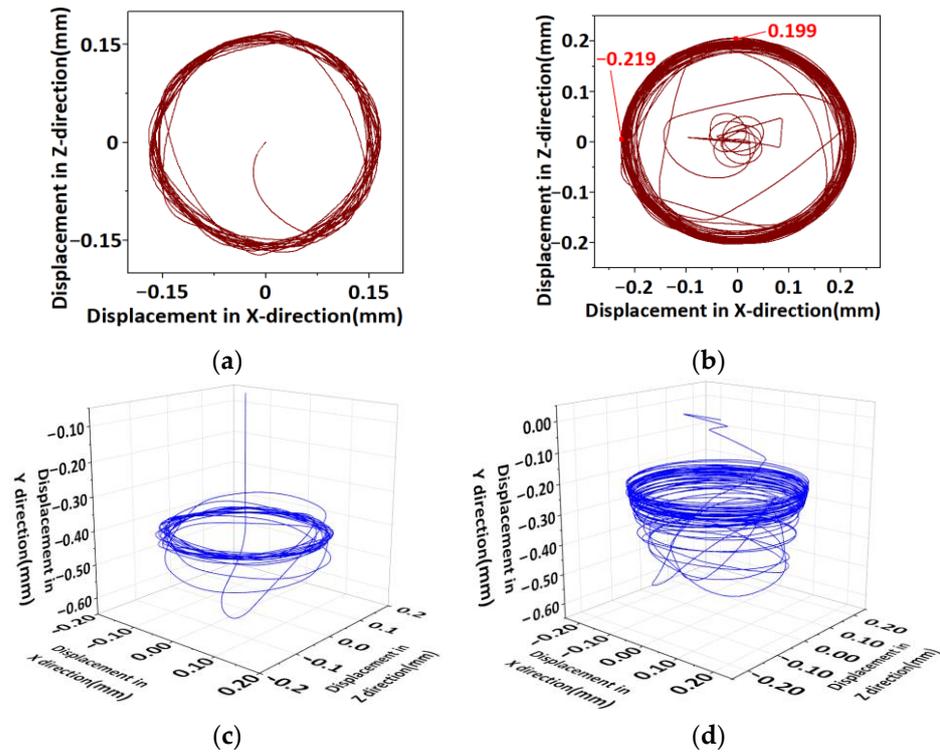
Figure 5. Comparison of eccentric-free and eccentric 0.05° rotor axis. (**a**) Non-eccentric rotor radial axial displacement; (**b**) Radial axial displacement of the eccentric rotor; (**c**) Space-wise displacement of the non-eccentric rotor axis; (**d**) The spatial displacement of the eccentric rotor axis.
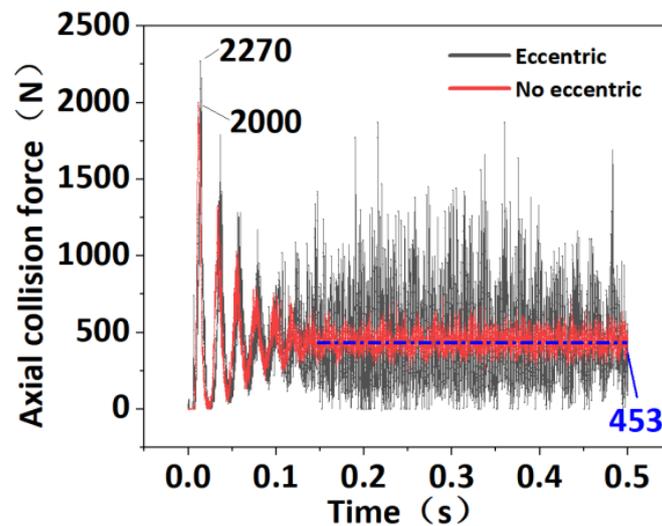
Figure 6. Comparison of the trend of the axial collision force at 0.05° with and without eccentricity.
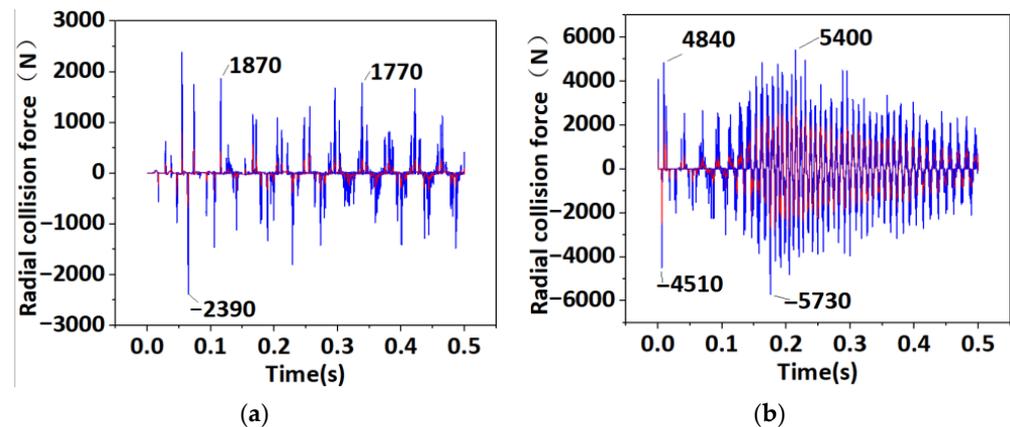
Figure 7. Comparison of non-eccentric and eccentric 0.05° rotor radial collision force. (**a**) Non-eccentric rotor radial collision force; (**b**) Radial collision force of the eccentric rotor.

As can be seen from Figure 5a,c, the axis locus after rotor fall and collision under a non-eccentric working condition is relatively stable, and there is almost no chaotic trajectory in the circle. The motion trajectory of the rotor in the radial direction is approximately fitted to a circle with a diameter of 0.158 mm, which has a small motion amplitude and fast stabilization speed.

According to Figure 5b,d, in the radial plane of the trajectory, the ellipse fitted by the rotor trajectory has a long axis of 0.225 mm and a short axis of 0.2 mm. Because the radial protection clearance of the magnetic levitation bearing system is 0.2 mm, it can be seen that the rotor shows a polygonal trajectory due to rebound under eccentric conditions, which indicates that the rotor will have friction collision with the inner ring of the protective bearing in the radial direction. The rotor falls behind, in the axial upward, after the collision bounce height fluctuation. It can be seen that the track-intensive area is concentrated in the upper part, and the overall lower track clutter is very significant. This is caused by the oblique elliptic surface of the drop space trajectory of the rotor axis under eccentric conditions.

Figure 6 shows the trend comparison of the maximum axial impact force on the rotor under the two working conditions over time. The maximum impact force appears in the first impact. It is observed that the falling collision force (red line) in unbiased conditions will soon stabilize at around rotor gravity of 450 N, as shown in the blue line in the figure. The maximum impact force of the rotor falling 2270 N under eccentric conditions is 14% higher than that under non-eccentric conditions, and its variation trend before 0.1 s is similar to that under non-eccentric conditions. In 0.1 s~0.5 s, the collision force with an average value of 967 N, which is 100% higher than that of the former, continues to appear and does not stabilize to 450 N at 0.5 s.

Corresponding to Figure 5d, it can be seen that the increase of axial impact force under eccentric conditions will increase the reaction force on the rotor from the bearing inner ring, resulting in the rise of the rotor rebound height. The rotor axis locus is no longer a circle in a horizontal radial direction but appears as an oblique elliptic plane in space. As the value of the late collision force continues to be high, the rotor rebound height is still higher than that in the non-eccentric condition and finally presents the trajectory as shown in Figure 5d.

It can be seen from Figure 7a that the maximum radial impact force does not occur in the first impact. Compared with the axial impact force, the maximum radial impact force does not gradually stabilize with time. According to Figure 5a, the maximum displacement of the rotor axis locus is 0.158 mm, less than the radial protection clearance of 0.2 mm. Furthermore, because the inner ring of the protective bearing also has a radial floating instability phenomenon, the rotor and the inner ring have periodic collisions, resulting in radial collision force. According to Figure 7b, the high numerical radial impact force of the rotor falling under eccentric conditions appears before 0.1 s, while it is very intensive

after 0.1 s. The peak radial force of 5400 N is 130% higher than that of 2390 N in non-eccentric conditions, and the total radial force value is 140% higher than that in non-eccentric conditions. This is the elliptical trajectory caused by the superimposed rotation and revolution of the rotor. When the linear velocity of the rotor axis increases, the centrifugal force increases, and the radial impact component is generated after the collision between the rotor and the inner ring, which makes the eccentric radial impact force multiply compared with the non-eccentric conditions.

It can also be seen from Figure 5b that the radial impact force generated by the collision between the front rotor and the inner ring of the protective bearing at 0.1 s makes the trajectory of the axis center have a polygon trajectory. As shown in Figure 7b, the radial collision force of the latter part is dense, and the collision between the rotor and the inner ring leads to a higher frequency of polygon trajectories, which will make the effect of the quasi-synthetic circle of the center of mass worse. As shown in Figure 5b, the moving distance of the centroid on the radial plane increases from 0.15 mm to 0.219 mm; that is, the long axis of the trajectory shape is 0.219 mm, and the short axis is 0.199 mm, which approximates to form an ellipse.

In conclusion, under certain initial conditions of the external boundary, the spatial form of rotor eccentricity makes the drop impact force of the rotor colliding with the inner ring of the protective bearing produce axial and radial impact components. In the late 0.1 s, the values of both remain high, and the relative slip between the inner ring and the rotor also causes changes in radial force and abnormal vibration, accompanied by a certain reverse vorticity [27–29]. This will lead to a larger range of longitudinal rebound displacement or penetration displacement and a larger unidirectional radial displacement than the trajectory of the non-eccentric drop conditions. Finally, the elliptic trajectory is synthesized, and a collision occurs, which is more unstable.

It can be seen that the rotor drop under the actual eccentric condition has greater impact-wear on the protective bearing. Under the conditions of heavy load, high speed, and large gap between tooling, it is easy to make the magnetic levitation system scrap and fail. The following will be analyzed and discussed from the following three aspects: the influence of rotor quality, rotational speed, and the gradient rise of axial protection clearance on the fall collision under the condition of five eccentric angles.

4.2. Effect of the Rotor Quality on the Collision

Table 2 shows the control parameters of working conditions with different rotor quality conditions, and five groups of control simulation are set.

**Table 2.** Input boundary conditions.

Name	1	2	3	4	5
Rotor quality (kg)	25	35	45	55	65
Axial protection clearance (mm)			0.25		
Rotor rotation speed (r/min)			20,000		

It can be seen from Figure 8a that the distance between the position of the final stop and the zero of the rotor in the non-eccentric condition increases with the increase of the rotor quality. The trend of the axial displacement curve is similar to that of axial impact force under non-eccentric conditions in Figure 6. It can be seen from Figure 8b that the displacement trend of the rotor falling before 0.1 s in the eccentric condition is similar to that in the non-eccentric condition. After 0.1 s, the longitudinal rebound amplitude increases due to rotor collision. This corresponds to the phenomenon that the axial impact force remains high after 0.1 s under the eccentric working condition in Figure 6.
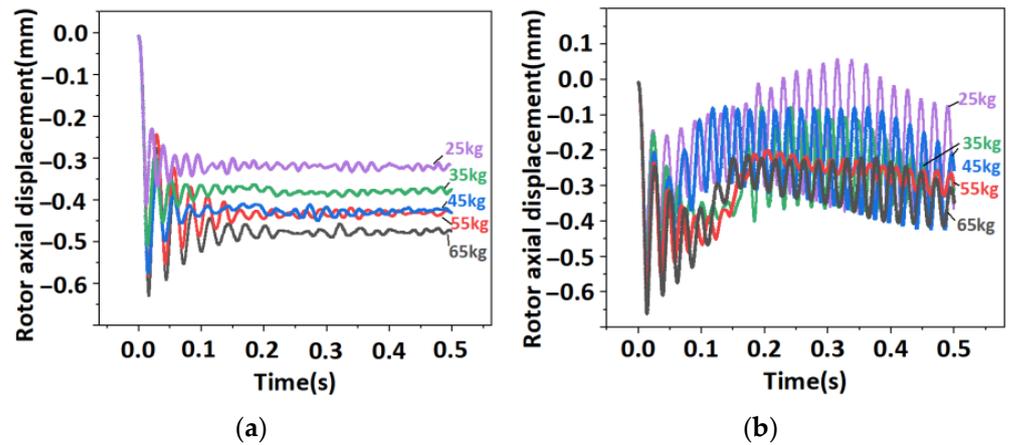
Figure 8. Comparison of non-eccentric and eccentric 0.05° rotor radial collision force. (**a**) Axial displacement of the rotor drops of different qualities under non-eccentric working conditions. (**b**) Axial displacement of rotor drops of different qualities at 0.05° eccentric conditions.

As can be seen from Figure 9a, the maximum axial displacement of rotor drop in both non-eccentric and eccentric conditions increases with the increase of rotor quality, and the maximum axial displacement in the eccentric condition is greater than that in the non-eccentric condition. Compared with the non-eccentric condition, the quality increases by 160%, and the displacement increases by 50%, indicating that this trend is nonlinear. In Figure 9b, it can be seen that the harmonic motion generated with rotor collision and rebound in the non-eccentric working condition within 0.2~0.5 s enters the stable stop state. With the increase of rotor quality, the depth amplitude is basically stable at 0.053 mm, while the average depth amplitude in the eccentric condition is increased by 350% compared with that in the non-eccentric condition, and the amplitude decreases with the increase of rotor quality [30].
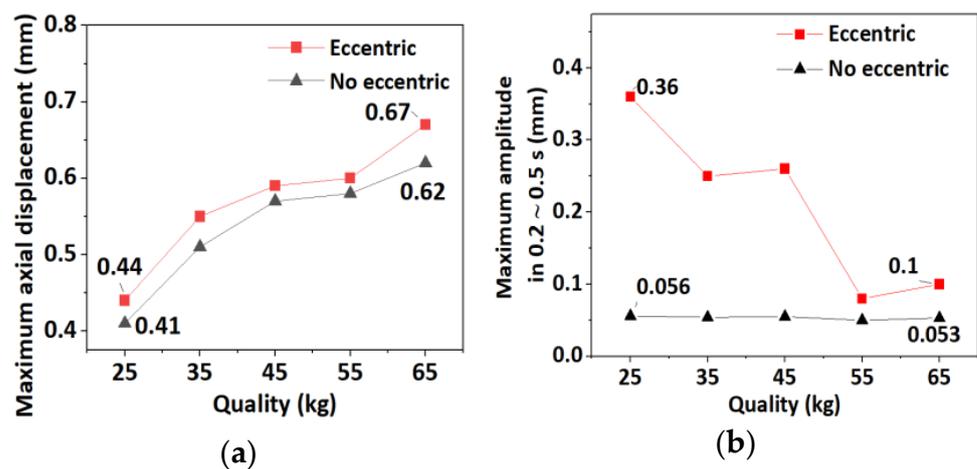
Figure 9. Comparison of maximum axial displacement and maximum amplitude of different quality rotor drops without eccentricity and eccentricity 0.05° working condition. (**a**) Comparison of the maximum axial displacement; (**b**) Comparison of the maximum amplitude within the 0.2~0.5 s.

The rotor rotates non-eccentric. According to the impulse formula $I = FT$, the quality increases, and the depth of impact into the inner ring deepens. According to Equation (20), the ball displacement B_{za} (Y+) increases, and the contact angle α increases. Due to the fixed outer ring, the inner ring of the protective bearing generates a displacement in the axial direction of (Y+); that is, the axial displacement of the rotor decreases so that the axial displacement becomes stable rapidly.

Compared with the non-eccentric condition, the greater the quality, the greater the impact of the rotor drop on the bearing inner ring in the eccentric condition, the deeper the intrusion displacement, the smaller the amplitude of rebound depth, but the overall is still greater than the non-eccentric condition.

Figure 10a shows the 3D color mapping surface of the axial impact force affected by different qualities under the eccentricity angle increased by five gradients (0.01~0.09°).
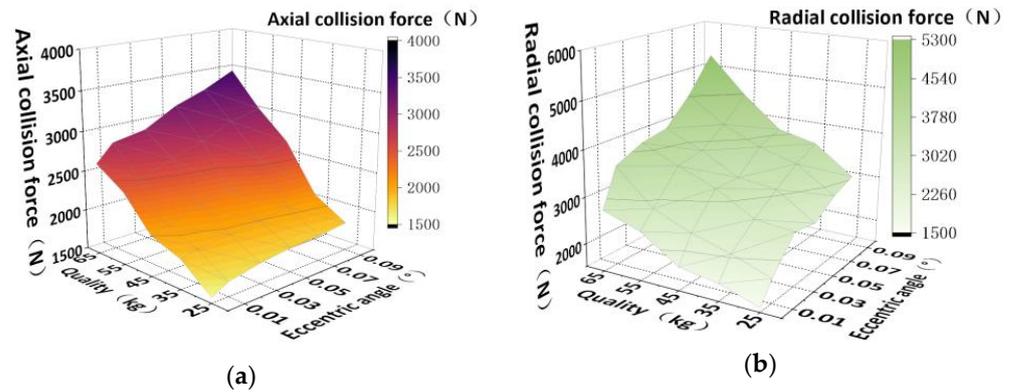

Figure 10. Axial and radial collision forces of quality on rotors with different speeds. (**a**) Maximum axial collision force; (**b**) Maximum radial collision force.

According to the gravity formula and the impulse formula, when other boundary conditions are fixed, the quality of the rotor increases, and the accumulated impulse of the rotor during the falling time will also increase, thus leading to the increase of the axial collision force between the rotor and the protective bearing. With the increase of eccentric angle, the maximum increase of axial impact force reaches 1790 N. According to Equation (8), with the increase of eccentric angle ζ, the axial protection clearance Δa between half of the rotor and the upper protective bearing increases, impulse increases, and the maximum axial impact force F_a increases. In other words, the increase in rotor eccentricity will affect the increase in axial impact force. The greater the rotor quality, the greater the impulse and the greater the axial impact force. As shown in Figure 11a, when the eccentric angle is 0.05° and the rotor quality increases by 150%, the axial impact force on the inner ring increases by 75% compared with the non-eccentric condition, which is similar, showing a nonlinear increase in general. Moreover, it is easy to see from Figure 11a that the eccentric drop impact force is greater than the non-eccentric condition.
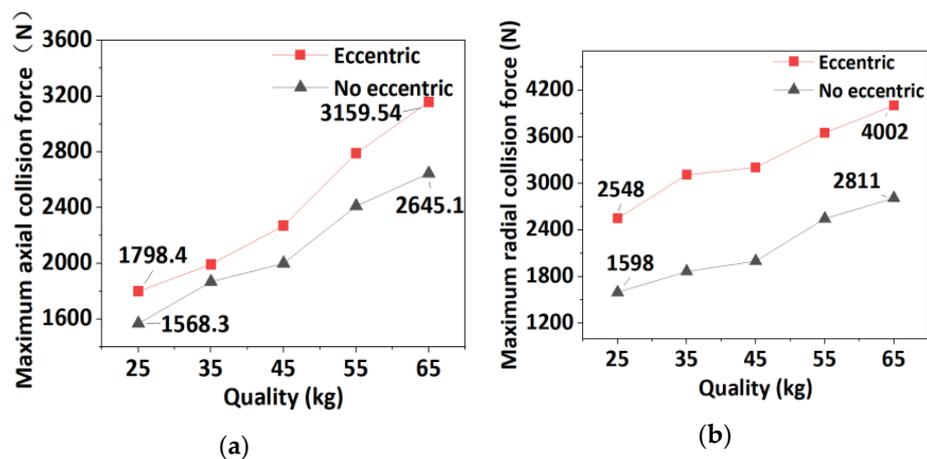

Figure 11. Comparison of maximum axial and radial collision forces. (**a**) Comparison of the maximum axial collision force of different quality rotor drops with an eccentricity of 0.05°; (**b**) Comparison of the maximum radial collision force of different quality rotor drops with an eccentricity of 0.05°.

Figure 10b is about the radial impact force, whose maximum increase reaches 3854 N, and the impact force also increases nonlinearly with the increase of quality and eccentricity angle. As shown in Figure 11b, under the condition of 0.05° eccentricity, the average value is 60% higher than that under the condition of non-eccentric eccentricity, the quality is 150% higher, and the radial impact force on the inner ring is 60% higher. Under eccentric conditions, along with the rotation and revolution of the rotor, the contact mode between the rotor and the inner ring changes from surface contact to local point contact, resulting in a local axial slip of the bearing inner ring and steel ball, constant changes in the rotation phase of the bearing inner ring, and the rotor falls to complete point contact collision. As the quality of the rotor increases, the component of gravity on the radial plane of the eccentric rotor also increases, leading to the component of the rotor on the radial plane of the inner ring. When the angle γ between the inner ring radial plane and the horizontal plane changes constantly, the high-frequency collision is repeated continuously; that is, the radial collision force between the two increases. With the increase of eccentric angle, it can be obtained from Equations (2) and (9) that the eccentric angle ζ increases, the transverse coordinate x_r of the rotor axis increases, the invasion depth τ_1 increases, and the normal velocity V_{n1} of the rotor relative to the inner ring of the bearing increases. According to Equation (8), the radial impact force F_{n1} between the rotor and the inner ring becomes larger if other fixed constants remain unchanged.

4.3. Influence of Rotor Speed on Collision

Table 3 shows the control parameters of different rotor speed conditions.

Table 3. Input boundary conditions.

Name	1	2	3	4	5
Rotor rotation speed (r/min)	5000	10,000	15,000	20,000	25,000
Rotor quality (kg)			45 kg		
Axial protection clearance (mm)			0.2		

In Figure 12a,b, it can be seen that the approximate fitting of the rotor axis displacement trajectory under non-eccentric working conditions is a circle with a diameter of about 0.155 mm, and there is no chaotic vibration trajectory in the trajectory, indicating that there is no collision with the bearing inner ring. However, the rotor speed increased from 5000 r/min to 25,000 r/min, and the degree of trajectory fitting was poor. In Figure 12c,d, it can be seen that, under eccentric conditions, the maximum displacement of the rotor's axial displacement track in both horizontal and vertical directions on the radial plane is wrong by a certain distance. This Figure approximates an ellipse with a major axis of 0.214 mm and a minor axis of 0.198 mm. As the speed reaches 25,000 r/min, the rotor collides with the inner ring of the bearing, resulting in a polygonal axis locus.


(a)   **(b)**
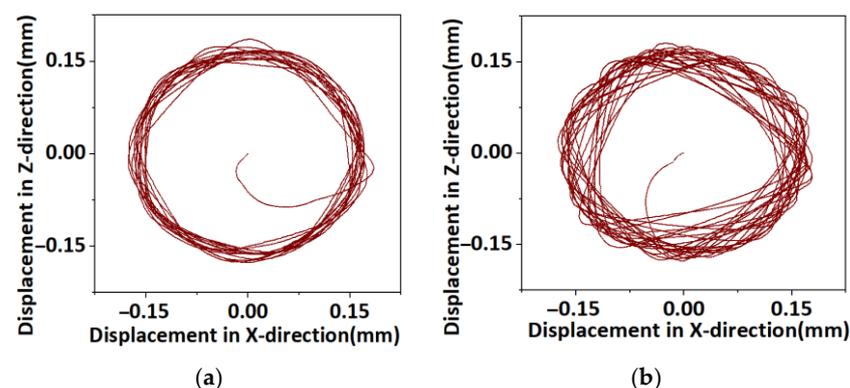
Figure 12. *Cont.*
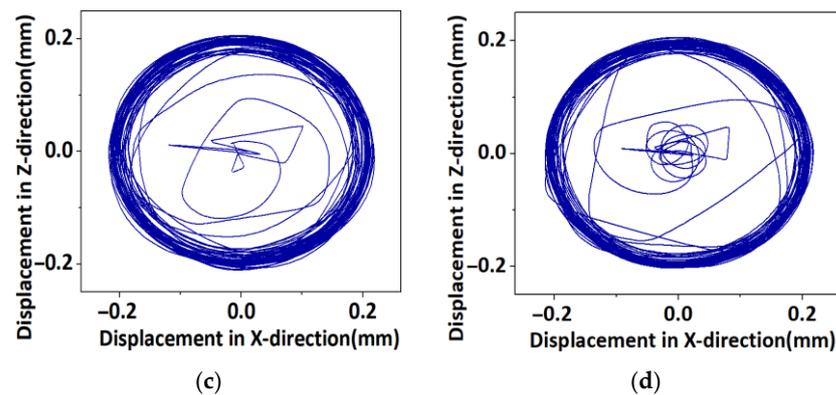
Figure 12. Radial displacement trajectory of non-eccentric and eccentric rotor shaft centers at different speeds. (**a**) 5000 r non-eccentric drop axis displacement; (**b**) 25,000 r non-eccentric drop axis displacement; (**c**) 5000 r eccentric 0.05° drop axis displacement; (**d**) 25,000 r eccentric 0.05° drop axis displacement.

When the rotor falls on the protective bearing, the speed of the inner ring of the protective bearing increases rapidly in a short time. The radial displacement of the rotor is mainly caused by the relative rotation of the rotor and the inner ring and the centrifugal force of the rotor. As the rotational speed increases, the centrifugal force increases, and the relative motion velocity of the two increases. As can be seen from Figure 4, the radial force F_x generated by friction increases, leading to the change of rotor force time, resulting in trajectory disturbance. Under eccentric conditions, the radial force direction changes irregularly due to the collision between the rotor and the inner ring, which is the reason for the poor fitting degree of the rotor trajectory.

Figure 13 shows the trend diagram of axial impact forces of rotors at different speeds under non-eccentric and eccentric conditions. According to the mathematical model established by Equation (10) and indirectly verified by Figure 13a, there is no obvious correlation between the maximum axial impact force and the non-eccentric rotor speed [24,25], and the maximum axial impact force is maintained around 2250 N. Figure 13b shows that the rotor and bearing inner ring under eccentric conditions increase from 5000 r/min to 25,000 r/min, and the axial impact force increases from 1918.4 N to 2186.65 N.
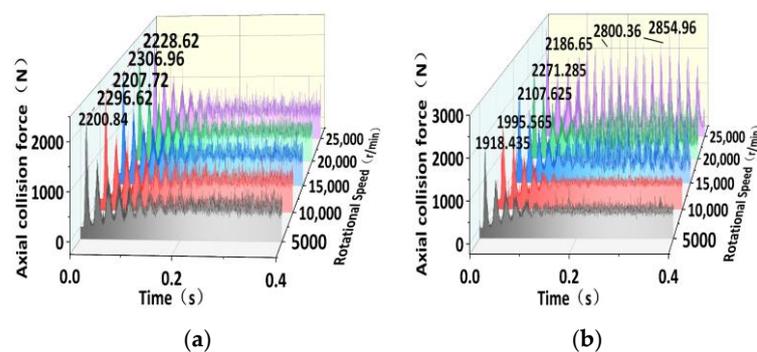
Figure 13. Comparison of axial collision forces between non-eccentric and eccentric rotors at different speeds. (**a**) Non-eccentric fall axial collision force; (**b**) Eccentricity 0.05° drop axial collision force.

It can be seen that the axial collision force corresponding to each speed decreases slightly, and the stability degree of the collision force trend in the late period is not as good as that in the non-eccentric condition. The increase in the speed is accompanied by periodic high-value collision forces, such as the appearance of 2800.36 N and 2854.96 N.

As the speed increases, the kinetic energy of the rotor increases.

In non-eccentric working conditions, this part of the energy is transferred to the bearing or consumed only through contact friction. The friction factor μ, rotor quality m, axial protection clearance Δh, and other conditions do not change; that is, the friction force of the rotor and the gravitational potential energy of the rotor itself do not change, and the maximum impact force basically does not change with the change of rotor speed when the rotor starts to fall.

Under eccentric conditions, according to gravity formula $G = mg$ and impulse formula $I = FT$, part of the axial protection clearance decreases, and part of it increases. When the rotor quality is constant, the accumulated impulse of the part of the rotor with small protection clearance decreases, and the impact force decreases. However, when the protection gap is large, the cumulative impulse increases and the impact force increases, and the change trend of the impact force is periodic. As the rotational speed increases, the impact force does not change obviously; that is, it has little effect on the axial impact force.

Figure 14a shows the axial impact force generated by the rotor falls at different speeds under the condition of five declination gradients (0.01~0.09°), and its maximum increase is about 610 N. As can be seen from Figure 15a, with the increase in rotational speed, the maximum axial impact force under non-eccentric conditions is basically stable.
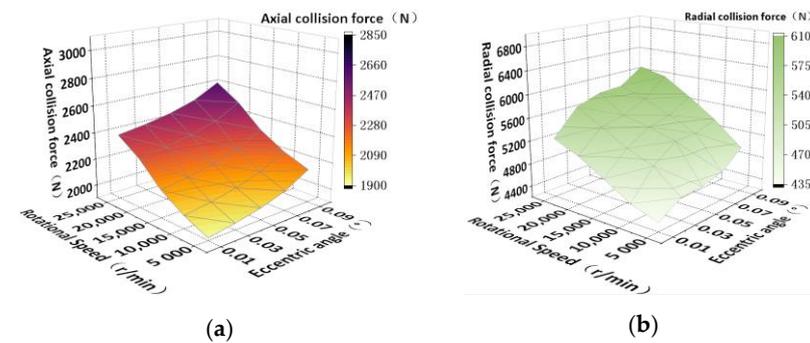
Figure 14. Eccentricity angle on the axial and radial collision force of rotor with different speeds. (**a**) Maximum axial collision force; (**b**) Maximum radial collision force.
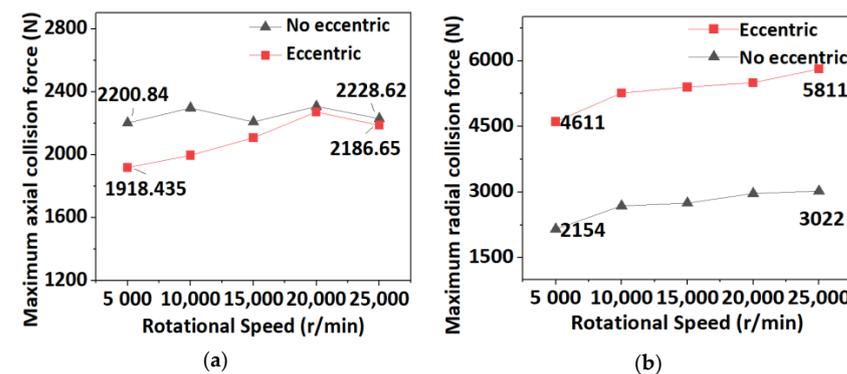
Figure 15. Comparison of maximum axial and radial collision forces under non-eccentric and eccentric working conditions. (**a**) Comparison of the maximum axial collision force of different speed rotor drops with eccentric 0.05°; (**b**) Comparison of the maximum radial collision force of different quality rotor drops with the eccentric 0.05°.

The corresponding maximum axial impact force is slightly less than the non-eccentric condition. With the increase in rotational speed, the nonlinear impact force increases slightly. The reasons have been explained above and will not be repeated here. As shown in Figure 14b, the maximum increase of radial impact force is about 1600 N. As shown in Figure 15b, the average maximum radial impact force under eccentric conditions is

110% higher than that under non-eccentric conditions, both of which are nonlinear and small increases.

According to Equations (2), (8)–(10), it can be seen that when the eccentric angle increases, the axial force F_a and radial force F_n both increase proportionally, and the radial impact force caused by the eccentric drop will increase the average force of the inner ring and steel ball, and the offset in the x and y directions of the inner ring will increase. According to Formula (3), with the increase of x_{b1} and y_{b1}, the relative compressive deformation between the inner ring and the steel ball increases τ_2; that is, the penetration depth of the channel between the protective bearing rolling body and the inner and outer ring increases, resulting in bearing pitting or fish-scale fatigue surface peeling, and reducing the life of the protective bearing [31,32].

4.4. Effect of Axial Protective Clearance on Collision

Table 4 shows the different control parameters of rotor speed conditions, with four sets of control simulations, and the eccentric angle is still five gradients.

Table 4. Input boundary conditions.

Name	1	2	3	4
Axial protection clearance (mm)	0.1	0.15	0.2	0.25
Rotor quality (kg)		45		
Rotor rotation speed (r/min)		20,000		

Figure 16 shows the axial displacement diagram of the rotor falling under non-eccentric conditions. The displacement of the rotor axis in the radial plane of the protective bearing shows a polygonal trend. With the increase of axial protection clearance, the rotor rebound height increases. The spatial displacement after rotation of the axis presents an oblique elliptic trajectory, while the one presented in the radial plane is a synthetic circular trajectory with a diameter of about 0.168 mm, which is less than the radial protection clearance of 0.2 mm.
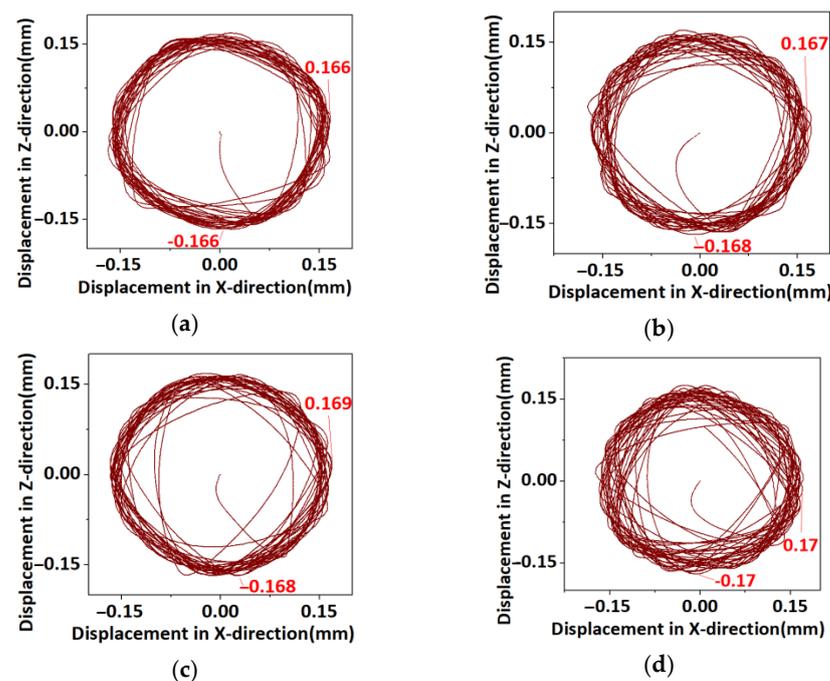

Figure 16. Radial axis displacement trajectory of the rotor under different axial protection gaps for non-eccentric working conditions. (**a**) 0.1 mm drop axis displacement; (**b**) 0.15 mm drop axis displacement; (**c**) 0.2 mm drop axis displacement; (**d**) 0.25 mm drop axis displacement.

As shown in Figure 17, the rotor axis presents a trend of collision rebound polygon variation in the radial plane of the protective bearing. The eccentricity of the rotor falls into the inner ring and superimposes its own rotation and revolution motion, lengthening the long axis of the space oblique elliptic trajectory. The direction of radial impact force changes constantly with the change of gyroscopic phase; the gyroscopic vibration of the rotor increases, and the variation amplitude of the radial displacement increases. With the increase of the axial protection clearance, the trajectory fitting growth axis is 0.21 mm, and the short axis is a 0.157 mm ellipse. This displacement has been greater than the radial protection clearance by 0.2 mm. With the increase of axial protection clearance, the radial collision between the rotor and the inner ring is severe, which will seriously affect the bearing life.


(a)

(b)

(c)

(d)
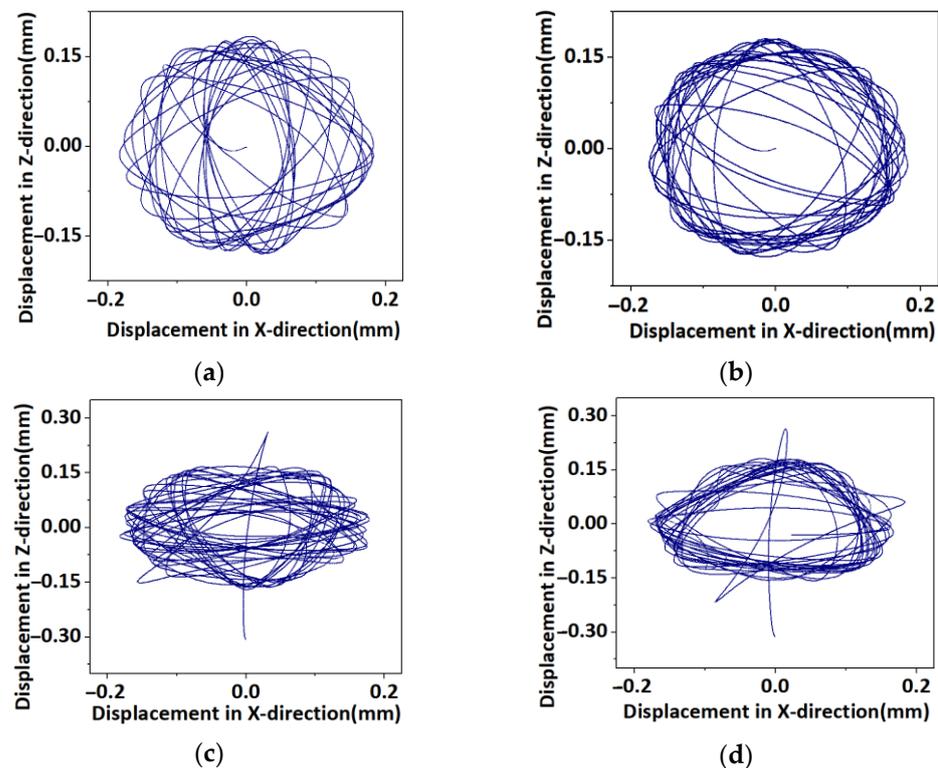
Figure 17. Radial axis displacement trajectory of eccentric 0.05° rotor under different axial protection clearance. (**a**) 0.1 mm Drop axis displacement; (**b**) 0.15 mm Drop axis displacement; (**c**) 0.2 mm Drop axis displacement; (**d**) 0.25 mm Drop axis displacement.

Figure 18a shows the axial impact force generated when the rotor with different axial protection clearance falls under the condition of five declination gradients (0.01°~0.09°). With the increase in the axial protection clearance and eccentricity angle, the maximum increase of axial impact force caused by rotor falling is 826 N. According to Figure 19a, with the increase of axial protection clearance, the average maximum axial impact force under eccentric conditions is 120 N larger than that under non-eccentric conditions, and the growth trend of both is similar. As the clearance Δh between the rotor and protective bearing increases, the initial energy of the rotor increases. According to the $h = 1/2\,gt^2$, $I = FT = mv$, the rotor drop time t increases, and the impulse and velocity are increased. Since the equivalent stiffness and damping of rotor and bearing are certain, the greater the speed at the moment of collision. The larger the eccentricity angle, the larger the contact pressure, the larger the deformation, and the larger the axial impact force.
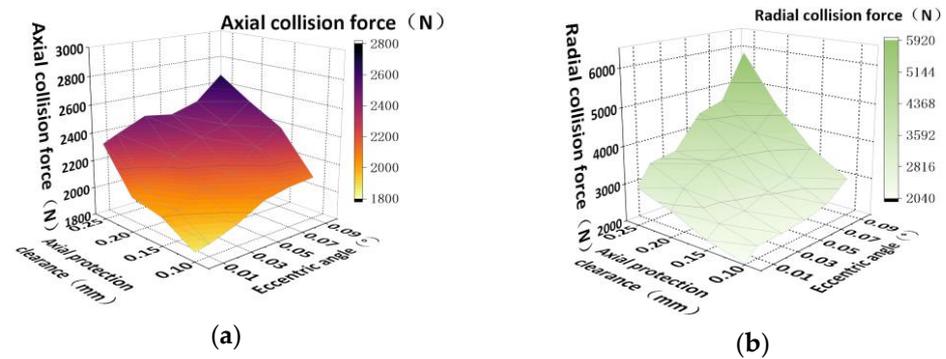
Figure 18. Eccentricity angle on the axial and radial collision forces of rotor drops with different axial clearances. (**a**) Maximum axial collision force; (**b**) Maximum radial collision force.
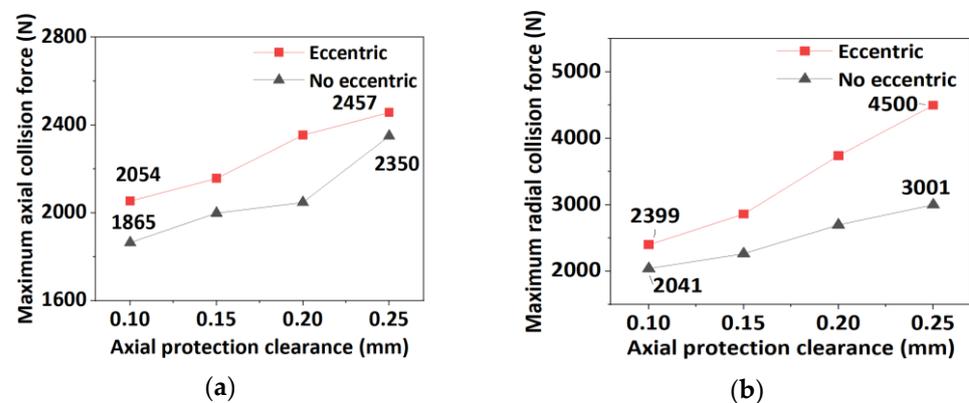
Figure 19. Comparison of maximum axial and radial collision forces under non-eccentric and eccentric working conditions. (**a**) Comparison of the maximum axial collision force of different axial protection clearance rotor drops under the 0.05° eccentric working condition; (**b**) Comparison of the maximum radial collision force of different axial protection gap rotor drops under the 0.05° eccentric working condition.

Figure 18b shows that the maximum radial impact force is 5896 N, twice the axial impact force. With the increase of eccentric angle, the maximum increase of radial impact force is 2806 N. As shown in Figure 19b, with the increase in axial protection clearance, the radial impact force increases by 1499 N and 1960 N in non-eccentric conditions as compared with that in non-eccentric conditions. Furthermore, the growth rate under eccentric conditions is obviously greater than that under non-eccentric conditions.

With the increase in the protection gap and impulse, it can be obtained from Equations (2) and (9) that the invasion depth τ_1 will deepen, and V_{n1} will increase. According to Equation (8), the radial impact force F_{n1} becomes larger. According to Figures 18 and 19, it can also be seen that the radial impact force increases with the increase of the axial protection clearance in the falling collision between the rotor and the bearing inner ring [28,33]. In other words, the fitting degree of the axial displacement trajectory under non-eccentric and eccentric conditions is also affected by the axial protection clearance.

5. Discussion of Drop Experiment

To simulate the drop performance of the eccentric rotor more in line with actual working conditions, a vertical rotor non-eccentric drop test was conducted using the protective bearing life test machine of the magnetic levitation bearing system shown in Figure 20. The 45 kg eccentric rotor speed rises with a 5, 10, 15, and 20 kr/min gradient. The protective bearing is a face-to-face mounted 71913C angular contact ball bearing, and the rest of the fall conditions are the same as the previous Table 3, and the rotor axis trajectory index is measured in real-time.
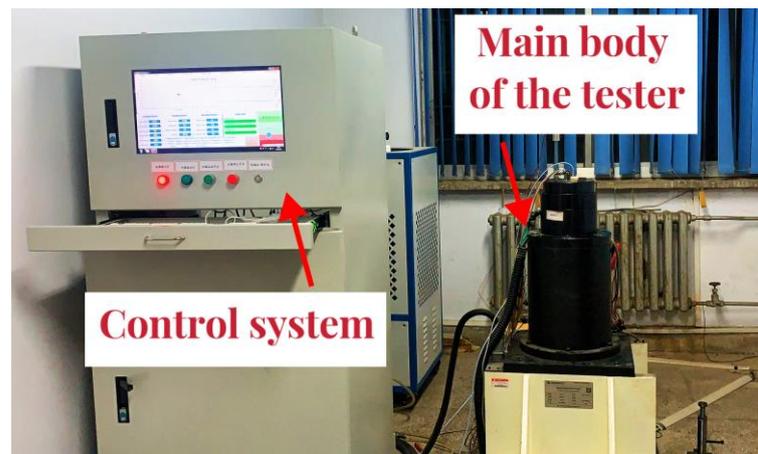
Figure 20. Life tester of auxiliary bearing for the active magnetic bearing system.

Figure 21 shows the radial axis displacement trajectory of the rotor set at different rotational speeds during the test; as the rotor speed increases, the degree of radial axis trajectory fitting into the circle gradually becomes worse, and the internal chaotic trajectory of the trajectory increases, and the rotor quality center trajectory in the radial direction has contact collision with the inner surface of the inner ring, resulting in the rotor in the process of axial collision rebound, while the velocity component of the rotor radial rebound exists. From the maximum diameter of the following four circular trajectory diagrams, it can be seen that as the rotor speed increases from 5 kr/min to 20 kr/min, the maximum displacement of the rotor radial center of quality increases from 0.15 mm to 0.18 mm, indicating that the rotor dynamic balance accuracy decreases as the speed increases. From the trajectory, this is consistent with the simulation results of the eccentric rotor above.
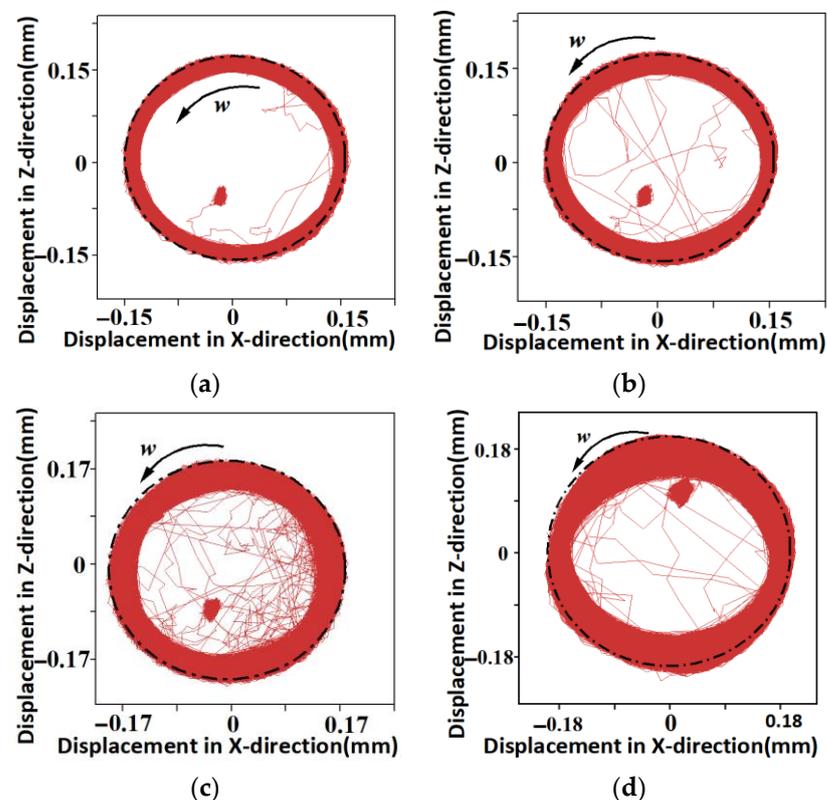

Figure 21. The centroid trajectory of rotors at different speeds in the process of falling collision. (**a**) 5 kr/min; (**b**) 10 kr/min; (**c**) 15 kr/min; (**d**) 20 kr/min.

In this paper, the impact force of the outer ring of the protective bearing is tested by the pressure sensor. As shown in Figure 22, sensor A and sensor B are symmetrically arranged at the bottom of the large end of the outer ring of the protective bearing. The outer ring is pressed and fixed by the pressing force exerted by the testing machine tooling, which conforms to the simulation model established above. The inner ring of the protective bearing is impacted by the rotor drop, and the axial impact force is transmitted to the outer ring through the rolling body so as to realize the change trend of the impact force indirectly. By comparison with Figures 6 and 23, it can be seen that, under the condition of the eccentric rotor, which is more in line with actual conditions, the maximum impact force of the outer ring is 979.477 N, and the average value of 212.71 N under stable conditions; both are about 1/2 of the corresponding force of the inner ring.
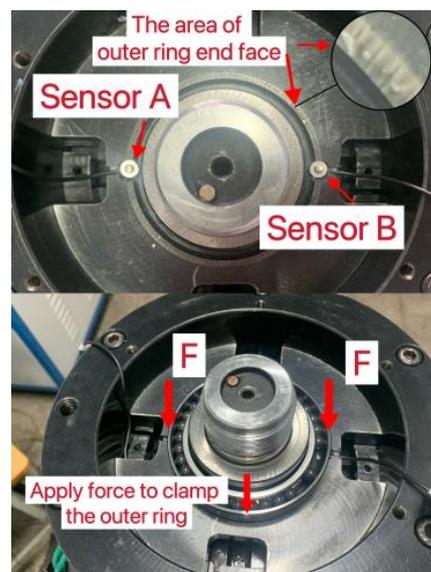

Figure 22. Installation diagram of axial collision force sensor.
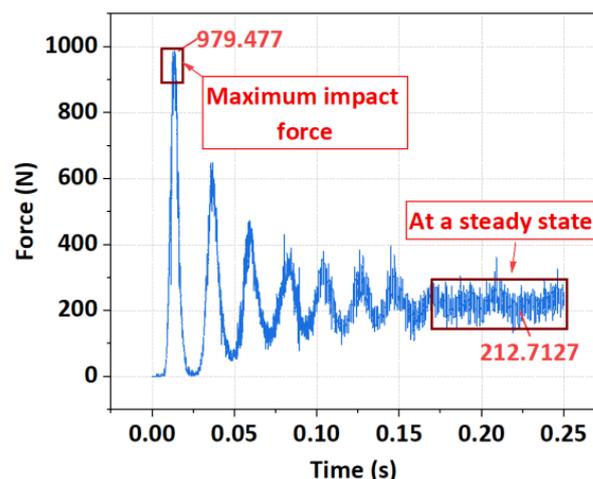

Figure 23. Simulation results of collision force on the outer ring.

As shown in Figure 24, according to the above experimental machine modification and simulation analysis results, the impact force of the outer ring of the protective bearing is tested. As shown in Figure 24a, the experimental data curve is divided into four stages: Rest, Rotor suspension acceleration, Falling collision stage, and Steady-state. The 389.1 N in the static stage in Figure 24a includes the outer ring force F= about 190 N and the dead weight of half of the rotor $G_{1/2}$ = 200 N. 192.4 N of the rotor suspension acceleration stage

only includes the outer ring force F = 190 N of testing machine tooling. The drop collision stage of 1169.7 N includes the outer ring pressing force F_O = 190 N and the maximum impact force F_{max} = 979.7 N. The mean value of 372.4 in the stable stage corresponds to the force value in the static stage.
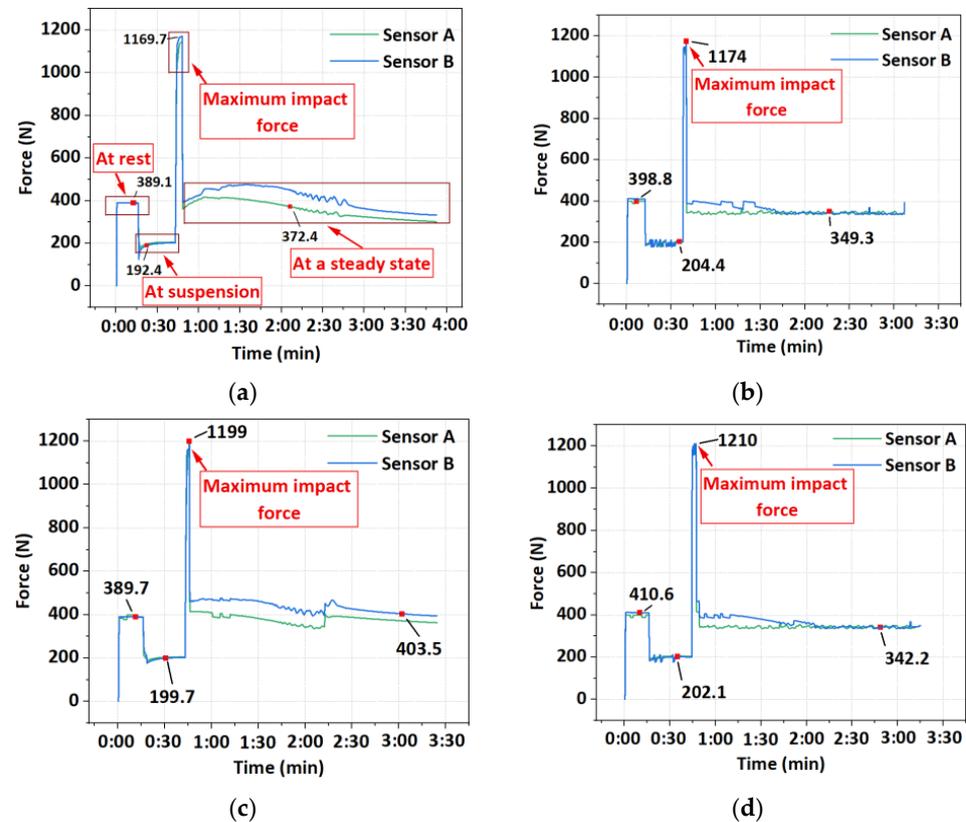
Figure 24. Force on the outer ring of the protective bearing with increasing speed. (**a**) 5 kr/min; (**b**) 10 kr/min; (**c**) 15 kr/min; (**d**) 20 kr/min.

Pay attention to the four figures in Figure 24. The rotor falls in the eccentric state, which is more consistent with the actual working condition. It can be seen that as the rotor speed increases from 5 kr/min to 20 kr/min, the force values of 1169.7 N, 1174 N, 1199 N, and 1210 N also rise gradient-wise. By comparison with Figure 13b above, it can be seen that the trend of simulation and experimental results is consistent and corresponding. In addition, after the four force values minus the outer ring force F_O = 190 N, compared with Figure 23, the maximum collision force F_{max} corresponds to the simulation, all of which are about 980 N. These are close to the simulation results above and also verify the accuracy of the self-programming simulation model above.

Figure 25 shows the appearance of the inner ring of the protective bearing after the collision of the eccentric rotor drop at different rotational speeds. 5 kr/min of the inner ring has no obvious changes; observe 20 kr/min of the inner ring, the ceramic ball, by the axial impact of running scratches the inner ring groove, indentation is obvious, the rotor drops to the inner ring end surface of the bearing, the speed is too high, deceleration time is extended, the inner ring end surface also reveals obvious scratches, resulting in the ceramic ball and groove, the ceramic ball and the groove, the friction between the rotor collision pad and the inner ring end surface increases, generating intense heat, affecting the protection of the bearing against falling performance and service life.

Figure 25. The appearance of the inner ring of the protective bearing at 20 kr/min and 5 kr/min operating conditions.

6. Conclusions

This paper first compares and discusses the rotor drop impact characteristics under eccentric and non-eccentric working conditions and then explores and analyzes the rotor axial displacement and axial and radial impact forces under three working parameters (quality, speed, axial protection clearance). The results are as follows:

(1) Under eccentric conditions, an ellipse with a long axis of 0.225 mm larger than the radial protection clearance is synthesized after the rotor falls. The axis locus under non-eccentric conditions is a circle with a diameter of 0.158 mm. Compared with the non-eccentric condition, the radial impact force increases by 140% on average, and the maximum axial impact force increases by 14%. Both of them produce high collision force, which is close to the maximum value continuously after 0.1 s. The results show that the eccentric condition has a great adverse effect on the stability of the axial displacement of the rotor, and both axial and radial impact forces are multiplied.

(2) With the increase in rotor quality, compared with the non-eccentric condition, the average increase of rotor axial drop displacement in the eccentric condition is 0.04 mm, and the amplitude in depth is increased by 350%. With the increase in eccentric angle, the axial impact force increases by 1.75 times, and the radial impact force increases by 60%. The results show that the change of quality can deepen the axial penetration depth after the rotor drops under eccentric conditions and has a great influence on the axial and radial impact force.

(3) With the increase in rotor speed, the maximum axial impact force decreases slightly, and the radial impact force increases by 110% compared with the non-eccentric condition. The maximum axial impact force changes slightly under non-eccentric conditions. An ellipse with a long axis of 0.214 mm, which is larger than the radial protection clearance, is synthesized from the rotor drop trajectory under eccentric conditions. The results show that the increase in rotational speed has little effect on the axial impact force, but a great effect on the radial impact force, and the collision between the rotor and the inner ring leads to the trajectory disorder.

(4) With the increase of the axial protection clearance Δh, the pseudo-circle degree of the rotor axis displacement trajectory becomes worse in both non-eccentric and eccentric conditions. The trajectory under eccentric conditions is an ellipse with a radial fitting growth axis of 0.21 mm larger than the radial protection clearance of 0.2 mm. With the increase of eccentric angle, the average increase of the maximum axial force is 120 N, and the average increase of the maximum radial force is two times. The results show that the increase of the axial protection clearance will cause the disturbance of

the radial displacement trajectory of the rotor, and the axial impact force will increase slightly, but the radial impact force will be greatly affected.

(5) After trial verification, the rotor speed increases the rotor radial axis trajectory to the degree of poor rounding and radial displacement from 0.15 mm to 0.18 mm. The force of the protective bearing outer ring increased from 1169.7 N to 1210 N. The inner ring groove and end face scratching are obvious, and frictional heat increases.

The eccentric working condition is 20~150% higher than the collision force without eccentric working conditions, and the shaft offset is larger than the radial protection gap of 0.2 mm, which indicates that the eccentric inclination of the rotor will cause greater impact damage to the bearing. Tsinghua University [15] studied the rotor drop of a heavy vertical magnetic bearing onto a protective bearing. In the experiment, the axial impact force and heating of vertical rotor falling were investigated. The change of axial impact force can only be measured indirectly by the sensor in the rotor drop experiment. In the future, intelligent, protective bearings may be used for temperature measurement or direct measurement of axial impact force so as to improve the impact resistance of protective bearings more effectively. Yang, G. also analyzed the inclination of the vertical rotor around the horizontal plane and proposed a detailed model of the vertical rotor falling process considering the inclination of rotation around the x and y axes [19]. He accurately predicted the dynamic behavior of the rotor in vertical descent. In his study on the axial impact force of rotor dropping, the influence of the friction coefficient is very weak, and the axial aerodynamic force tends to increase the peak axial contact force.

In view of the large impact force value in the case of eccentricity mentioned above, such high impact force exists objectively because the eccentricity error is unavoidable in actual manufacturing or the high-speed rotation of the motor-driven rotor [34]. This can reduce the axial impact force of the rotor by improving the rotor operating condition parameters and the structural parameters of the protective bearing, such as axial protection clearance, rotor dynamic balance accuracy, the number of ball fillings in the bearing, whether there is a cage or not, and changing the ring material, which will be a very meaningful study. The rotor of the vertical magnetic suspension bearing system will keep the eccentric condition when running. In this paper, the dynamic process of rotor eccentric drop is analyzed innovatively in the field of magnetic bearing research, and it is concluded that the actual impact of an eccentric rotor on the system is more serious than that of the non-eccentric rotor in all aspects. Therefore, before practical applications or tests, high requirements are put forward for the improvement of the overall impact resistance of protective bearings and the design of rotor dynamic balance precision. Future research in the field of impact protective bearings should focus on the rotor eccentricity drop conditions. This paper provides a reference for the research in this field. In addition, the research results of this paper will be helpful to the further improvement of protective bearing design and engineering application.

Author Contributions: Conceptualization, X.P. and D.Z.; methodology, X.P.; software, D.Z.; validation, D.Z. and X.W.; formal analysis, M.Q.; investigation, D.Z.; resources, D.W.; data curation, X.P. and D.Z.; writing—original draft preparation, X.P. and D.Z.; writing—review and editing, X.P. and D.Z.; visualization, D.W. and X.W.; supervision, X.P.; project administration, X.P. and D.Z.; funding acquisition, D.W. All authors have read and agreed to the published version of the manuscript.

Conflicts of Interest: The authors declare no conflict of interest.

References

1. Gao, H.; Xu, L. Real-time Feed-forward Force Compensation for Active Magnetic Bearings System Based on H∞ Controller. *Chin. J. Mech. Eng.* **2011**, *24*, 58–66. [CrossRef]
2. Zhang, W.; Zhu, H.; Yuan, Y. Study on Key Technologies and Applications of Magnetic Bearings. *Trans. China Electrotech. Soc.* **2015**, *30*, 12–20.

3.	Xia, X. Dynamics of Magnetic Suspended Rotor Drop on Auto Eliminating Clearance Auxiliary Bearings. Master's Thesis, Nanjing University of Aeronautics and Astronautics, Nanjing, China, 2014.

4.	Khanlo, H.M.; Ghayour, M.; Ebrahimi, R. Chaotic Vibration Analysis of a Coaxial Rotor System in Active Magnetic Bearings and Contact With Auxiliary Bearings. *J. Comput. Nonlinear Dyn.* **2016**, *12*, 031012.

5.	Wu, G.; Lu, B.; He, D.; Song, C. The research and analysis on critical speed of auxiliary support system for magnetic suspension wind turbine. *Mod. Manuf. Eng.* **2018**, *458*, 14.

6.	Kong, Y.; Xue, Y.; Ye, J.; Jiao, Y. Impact Characteristics of Vertical Rotor Dropping on Auxiliary Bearings. *Mach. Tool Hydraul.* **2021**, *49*, 6–11.

7.	Zhu, Y.; Jin, C.; Xu, L. Effect of different elastic ring installation locations in catcher bearing system on rotor drop dynamic responses. *J. Aerosp. Power* **2012**, *27*, 1671–1680.

8.	Wei, P.; Wang, Y.; Yang, Y.; Yan, L.; Xu, L. An analysis of the contact force between a floating rotor and a retainer bearing after rotor drop. *J. Vib. Shock* **2018**, *37*, 251–258.

9.	Zhao, J.; Yang, G.; Li, Y.; Yu, S.; Xu, L. Numerical Analysis of Magnetically Suspended Rotor in HTR-10 Helium Circulator Being Dropped into Auxiliary Bearings. *Nucl. Power Eng.* **2012**, *33*, 61–64.

10.	Keogh, P.S.; Yong, W.Y. Thermal Assessment of Dynamic Rotor/Auxiliary Bearing Contact Events. *J. Tribol.* **2006**, *129*, 143–152. [CrossRef]

11.	Ma, Z.; Zhao, D.; Ni, Y. The Dynamic Response Analysis of Floating Rotor-Touchdown Bearing in AMB System. *Bearing* **2022**, *65*, 1–9.

12.	Ma, L.; Lin, M.; Shijun, W.; Peng, W. Research on the Dynamic Characteristics of Magnetic Bearing-rotor System with Auxiliary Bearing. *J. Phys. Conf. Ser.* **2020**, *1637*, 012140. [CrossRef]

13.	Yang, G.; Xu, Y.; Shi, Z.; Gu, H. Characteristic analysis of rotor dynamics and experiments of active magnetic bearing for HTR-10GT. *Nucl. Eng. Des.* **2006**, *237*, 1363–1371.

14.	Zhu, C. Nonlinear dynamics of rotor drop on rolling element backup bearings after active magnetic bearings failure. *J. Mech. Eng.* **2006**, *7*, 196–202. [CrossRef]

15.	Li, Z.; Shi, Z.; Tie, X.; Yang, G.; Ren, W.; Yao, J.; Wang, Y.; Wang, Z. Failure Mechanism on Touchdown Bearing of Heavy Maglev Rotor Drop. *China Mech. Eng.* **2023**, *34*, 1009–1018.

16.	Altaf, S.; Mehmood, M.S.; Soomro, M.W. Advancement of Fault Diagnosis and Detection Process in Industrial Machine Environment. *J. Eng. Sci.* **2019**, *6*, D1–D8. [CrossRef]

17.	Lyu, M.; Liu, T.; Wang, Z.; Yan, S.; Jia, X.; Wang, Y. A control method of the rotor re-levitation for different orbit responses during touchdowns in active magnetic bearings. *Mech. Syst. Signal Process.* **2018**, *105*, 241–260. [CrossRef]

18.	Anna, T.; Enrico, M.; Andrea, R.; Alessandro, R.; Pierluca, D.A.; Amedeo, F.; Duccio, F.; Benjamin, D. Development and Experimental Validation of Auxiliary Rolling Bearing Models for Active Magnetic Bearings (AMBs) Applications. *Int. J. Rotat. Mach.* **2019**, *2019*, 4675286.

19.	Wang, Z.; Ding, H.; Chen, L. Modeling of a magnetic levitation energy harvesting system attaching a linear oscillator under multi-frequency excitation and its output power's influencing parametric analysis. *J. Vib. Shock* **2018**, *37*, 225–229.

20.	Fang, B.; Zhang, J.; Hong, J.; Yan, K. Research on the Nonlinear Stiffness Characteristics of Double-Row Angular Contact Ball Bearings under Different Working Conditions. *Lubricants* **2023**, *11*, 44. [CrossRef]

21.	Fumagalli, M.A.; Schweitzer, G.; Ulbrich, H. Modelling and Measurement Analysis of the Contact Interaction between a High Speed Rotor and Its Stator. Ph.D. Dissertation, ETH Zürich, Zürich, Switzerland, 1997.

22.	Neisi, N.; Sikanen, E.; Heikkinen, J.E.; Sopanen, J. Effect of off-sized balls on contact stresses in a touchdown bearing. *Tribol. Int.* **2018**, *120*, 340–349. [CrossRef]

23.	Liu, T.; Lyu, M.; Wang, Z.; Yan, S. An identification method of orbit responses rooting in vibration analysis of rotor during touchdowns of active magnetic bearings. *J. Sound Vib.* **2018**, *414*, 241–260. [CrossRef]

24.	Ma, S.; Yin, Y.; Chao, B.; Yan, K.; Fang, B.; Hong, J. A real-time coupling model of bearing-rotor system based on semi-flexible body element. *Int. J. Mech. Sci.* **2023**, *245*, 108098. [CrossRef]

25.	Inayat-Hussain, J.I. Nonlinear Dynamics of a Magnetically Supported Flexible Rotor in Auxiliary Bearings. *J. Phys. Conf. Ser.* **2020**, *1489*, 012015. [CrossRef]

26.	Yang, G.; Zhao, L.; Keogh, P.; Zhao, Y. Dynamic Analysis for the Rotor Drop Process and Its Application to a Vertically Levitated Rotor/Active Magnetic Bearing System. *J. Tribol.* **2017**, *139*, 041701.

27.	Wang, J.; Jia, X.; Zhang, K.; Xu, Y. Research on Dynamics of Magnetic Bearing Rotor Drop on Back-up Bearings. *China Mech. Eng.* **2022**, *33*, 2403–2413.

28.	Zhu, Y.; Jin, C.; Lian, C.; Zhen, Z. Dynamic Analysis of Vertical Rotor Drops Onto Deep Groove Ball Catcher Bearing. *Mach. Des. Res.* **2017**, *33*, 72–77.

29.	Yu, C.; Sun, Y.; Wang, H.; Shan, W.; Chen, Y.; Qiu, R. Dynamic analysis of magnetic bearing rotor dropping on radial and axial integrated auxiliary bearing. *Mech. Mach. Theory* **2019**, *140*, 622–640. [CrossRef]

30.	Heikkinen, J.E.; Ghalamchi, B.; Viitala, R.; Sopanen, J.; Juhanko, J.; Mikkola, A.; Kuosmanen, P. Vibration analysis of paper machine's asymmetric tube roll supported by spherical roller bearings. *Mech. Syst. Signal Process.* **2018**, *104*, 688–704. [CrossRef]

31.	Neisi, N.; Heikkinen, J.E.; Sopanen, J. Influence of surface waviness in the heat generation and thermal expansion of the touchdown bearing. *Eur. J. Mech. A Solids* **2018**, *74*, 34–37. [CrossRef]

32. Liu, X.; Zhou, Y.; Yan, X.; Zhao, J.; Shi, Z.; Chen, J.; Zhao, Y.; Yang, G. Experimental study on the novel rolling-sliding integrated auxiliary bearing in active magnetic bearing during rotor drop. *Ann. Nucl. Energy* **2020**, *136*, 107044. [CrossRef]

33. Wang, D.; Wang, N.; Chen, K. Fixed-point Rubbing Characteristics of Magnetic Suspended Dual-rotor Systems. *China Mech. Eng.* **2021**, *32*, 1686–1699.

34. Witanowski, Ł.; Breńkacz, Ł.; Szewczuk-Krypa, N.; Dorosińska-Komor, M.; Puchalski, B. Comparable analysis of PID controller settings in order to ensure reliable operation of active foil bearings. *Eksploatacja i Niezawodność Maint. Reliab.* **2022**, *24*, 377–385. [CrossRef]